mathematics

MDPI

Article

Smooth Tensor Multi-View Clustering on Well Logs via Hypergraph Topology and Concurrent Group Sparsity

Shengjiang Xu [1], Liwei Wang [1], Long Tian [1], Yinming Zhong [1], Junshan Wang [1], Wei Guo [2] and Haotian Zhang [2,*]

[1] Oil Production Technology Research Institute, Xinjiang Oilfield Company, China National Petroleum Corporation (CNPC), Karamay 834000, China; xusj@petrochina.com.cn (S.X.); yjwanglw@petrochina.com.cn (L.W.); tianlong@petrochina.com.cn (L.T.); zhongyinming@petrochina.com.cn (Y.Z.); wangjs2022@petrochina.com.cn (J.W.)

[2] School of Computer Science and Technology, Yibin University, Yibin 644000, China; guowei123@email.swu.edu.cn

* Correspondence: 2019116007@yibinu.edu.cn

Abstract

Multi-view clustering has emerged as a powerful approach to geological facies characterization because it can integrate heterogeneous well-log sequences. However, real-world well-log data are susceptible to severe localized environmental disturbances, such as borehole collapse. Moreover, conventional pairwise graph methods fail to capture the inherent high-order semantic correlations in sequential petrophysical data, whereas standard tensor methods indiscriminately retain high-frequency structural noise. To address these limitations, we propose Smooth Tensor Multi-View Clustering on Well Logs via Hypergraph Topology and Concurrent Group Sparsity (HTCGS). First, HTCGS introduces a source-view hypergraph topology-injection mechanism that propagates high-order geological manifold structures across heterogeneous modalities, thereby enabling robust geometric prealignment. Second, it employs a cross-view concurrent joint-group-sparsity regularizer that uses an $\ell_{2,1}$-norm penalty to separate localized anomalies into an explicit cross-view error matrix, thereby preserving the latent subspace. Finally, HTCGS applies the Smooth Tensor Nuclear Norm (STNN) to the purified latent features, which acts as a low-pass tensor filter to extract global consensus information reflecting macroscopic geological continuity. The resulting unified objective is efficiently optimized using the Alternating Direction Method of Multipliers (ADMM). Extensive experiments on five benchmark datasets, comprising four well-log datasets and one seismic-facies dataset, show that HTCGS outperforms six recent representative multi-view clustering baselines.

Keywords: multi-view clustering; well-log data; hypergraph topology; concurrent group sparsity; smooth tensor nuclear norm

MSC: 68T09; 68T10; 62H30

Check for updates

Academic Editors: Marjan Mernik and Jonathan Blackledge

Received: 19 August 2026
Revised: 14 September 2026
Accepted: 22 September 2026
Published: 22 October 2026

Copyright: © 2026 by the authors. Licensee MDPI, Basel, Switzerland. This article is an open access article distributed under the terms and conditions of the Creative Commons Attribution (CC BY) license.

1. Introduction

In many real-world machine-learning applications, data are collected from diverse sensors, observation domains, or feature extractors, producing multiple representations of each object that are collectively known as multi-view data [1–3]. For example, well-log data comprise various petrophysical sequences, such as natural gamma ray, acoustic transit time, and electrical resistivity measurements, each of which reflects a specific physical property at the same geological depth [4,5]. Multi-view clustering (MVC) partitions samples

into distinct categories by exploiting both consensus and complementary information across views [6,7]. Recent representative approaches include multi-view fusion based on extreme learning machines [8] and bidirectional probabilistic multi-graph learning and decomposition [9]. MVC methods have been widely studied for complex data structures and have achieved strong performance in applications such as image segmentation [10,11] and geological facies characterization [12–14].

An important and challenging application of MVC is the analysis of heterogeneous well-log sequences for geological characterization and downhole engineering [15–17]. In recent years, data-driven learning and clustering techniques have shown considerable potential for intelligent well-log and drilling interpretation. Representative applications include the unsupervised characterization of rock drillability [18], the prediction and evaluation of shale reservoir sweet spots [19], and the diagnosis and risk assessment of downhole anomalies, such as stuck pipes, through mechanism-guided data fusion [20,21]. For example, Meng et al. [22] applied multiresolution graph-based and dynamic clustering algorithms to conventional well logs to identify shale lithofacies and predict reservoir "sweet spots." To model complex data distributions and determine the number of clusters in diagenetic facies recognition, Zhang et al. [23] developed a multidimensional adaptive deep-clustering model based on an asymmetric autoencoder. Furthermore, recognizing the importance of vertical geological structure, Yang et al. [24] integrated Simple Linear Iterative Clustering with Transformers to capture stratigraphic continuity and dependencies among petrophysical features.

Despite the progress of existing MVC methods, three coupled research gaps remain when they are applied to heterogeneous downhole well-log data. First, conventional graph-based methods rely mainly on pairwise similarities and, therefore, cannot fully capture the high-order semantic correlations within structured petrophysical sequences. Second, commonly used elementwise noise models treat measurement anomalies independently and overlook synchronous environmental disturbances across multiple logging tools, such as the concurrent errors caused by localized borehole washouts. Consequently, these correlated distortions may be absorbed into the learned latent subspace. Third, standard tensor models do not explicitly distinguish structural information by frequency and may retain localized high-frequency measurement noise. These limitations have not been jointly addressed in a unified multi-view clustering formulation for sequential well-log analysis.

To address these coupled gaps, we propose Smooth Tensor Multi-View Clustering on Well Logs via Hypergraph Topology and Concurrent Group Sparsity (**HTCGS**). HTCGS integrates source-view hypergraph topology injection, cross-view concurrent group sparsity, and sample-wise smooth tensor filtering into a unified formulation. The overall architecture of HTCGS is shown in Figure 1. The main contributions of this paper are summarized as follows:

- **Source-View Hypergraph Topology Injection:** HTCGS extends traditional pairwise graphs by introducing a source-view hypergraph topology-injection mechanism. This module captures high-order data manifolds and propagates them across heterogeneous modalities, thereby achieving robust geometric prealignment.
- **Cross-View Concurrent Joint Group Sparsity:** To mitigate synchronous feature corruption, we formulate a cross-view concurrent joint-group-sparsity regularizer. By imposing a group-sparsity constraint on an explicitly defined error matrix, HTCGS adaptively isolates anomalies shared across views.
- **Robust Global Consensus via the STNN:** We employ the Smooth Tensor Nuclear Norm (STNN) as a low-pass filter that extracts a global low-rank consensus while mitigating the influence of localized high-frequency noise.

- **Efficient Optimization and Extensive Evaluation:** We design an efficient iterative algorithm for the unified objective. Experiments on four well-log datasets and one seismic-facies dataset demonstrate the advantages of HTCGS over six recent representative multi-view clustering methods.

The remainder of this paper is organized as follows. Sections 2 and 3 introduce the notation and review the related literature, respectively. Section 4 describes the proposed HTCGS framework and its optimization procedure. Section 5 presents experiments on real-world datasets, and Section 6 concludes the paper.

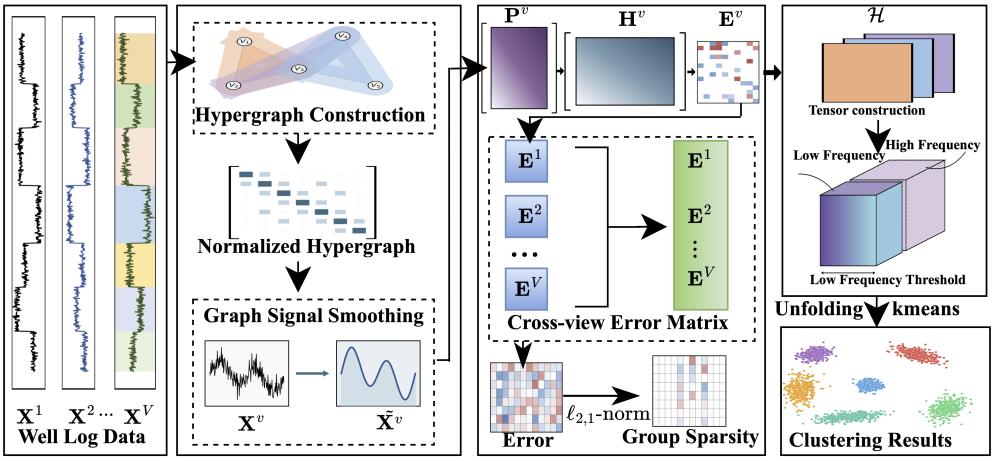


Figure 1. Overall architecture of the proposed HTCGS framework. The pipeline comprises three core mechanisms: (1) Hypergraph Topology Injection, which constructs a normalized hypergraph and smooths the raw multi-view well-log signals; (2) Concurrent Group Sparsity, which factorizes the smoothed data into latent representations $\boldsymbol{H}^v$ and isolates synchronous cross-view anomalies by applying the $\ell_{2,1}$-norm to the stacked error matrices; and (3) Smooth Tensor Filtering, which stacks the view-specific representations into a third-order tensor $\boldsymbol{\mathcal{H}}$ and applies a low-pass filter to remove high-frequency structural noise. Finally, K-means is applied to the optimized consensus representation to obtain the clustering labels.

2. Preliminaries and Notations

In this paper, scalars are denoted by regular letters (e.g., N), vectors by bold lowercase letters (e.g., $\boldsymbol{v}$), matrices by bold uppercase letters (e.g., $\boldsymbol{M}$), and third-order tensors by bold Euler script letters (e.g., $\boldsymbol{\mathcal{T}}$). The transpose of a matrix $\boldsymbol{M}$ is denoted by $\boldsymbol{M}^\top$. For a third-order tensor, $\hat{\boldsymbol{\mathcal{T}}}$ denotes its Fourier-domain representation obtained by applying the FFT along the third mode, and $\hat{\boldsymbol{\mathcal{T}}}^{(n)}$ denotes its n-th frontal slice. Table 1 summarizes the main notations frequently used in the HTCGS framework.

Table 1. Summary of frequently used notations.

Notation	Description
N, V, C	Numbers of samples, views, and clusters, respectively
d_v, d	Feature dimension of the v-th view and maximum feature dimension, where $d = \max_v d_v$
k, L	Number of nearest neighbors for hypergraph construction and low-frequency cutoff for the STNN, respectively
$\boldsymbol{X}^v, \tilde{\boldsymbol{X}}^v \in \mathbb{R}^{d_v \times N}$	Raw data and hypergraph-smoothed data of the v-th view
$\boldsymbol{P}^v \in \mathbb{R}^{d_v \times C}$	Orthogonal basis matrix of the v-th view
$\boldsymbol{H}^v \in \mathbb{R}^{C \times N}$	Latent representation of the v-th view
$\boldsymbol{E}^v \in \mathbb{R}^{d_v \times N}$	Error matrix of the v-th view
$\boldsymbol{E}_{\text{cat}}$	Concatenated cross-view error matrix
$\boldsymbol{\mathcal{H}}, \boldsymbol{\mathcal{Z}}, \boldsymbol{\mathcal{W}} \in \mathbb{R}^{C \times V \times N}$	Latent tensor, auxiliary tensor, and Lagrange multiplier tensor, respectively

Table 1. *Cont.*

Notation	Description
η, λ, γ	Topology-injection, joint-sparsity, and STNN regularization parameters, respectively
μ, ρ, ξ	ADMM penalty parameter, amplification factor, and convergence tolerance, respectively
$\Phi(\cdot)$	Operator that stacks view-specific representations into a third-order tensor
$\|\cdot\|_F, \|\cdot\|_{2,1}, \|\cdot\|_*$	Frobenius norm, $\ell_{2,1}$-norm, and matrix nuclear norm, respectively
$\|\mathcal{T}\|_{\text{STNN}}$	Smooth Tensor Nuclear Norm (STNN)

3. Related Work

This section reviews the technical evolution of MVC methodologies—categorized into graph-based, subspace-based, and deep learning-based paradigms—and highlights their theoretical limitations in processing complex geophysical sequences.

3.1. Graph-Based Multi-View Clustering

Graph-based MVC methods construct affinity graphs to capture data manifolds and then fuse them into a consensus graph for spectral clustering [25–27]. To reduce the prohibitive $\mathcal{O}(N^3)$ computational cost of traditional $N \times N$ graphs, recent studies have increasingly adopted anchor-based formulations. For example, Zhao et al. [28] incorporate the tensor Schatten p-norm into anchor graphs to capture complementary information and directly obtain cluster assignments. Another important research direction is improving the robustness and structural expressiveness of graph models. Wang et al. [29] use multi-view graph autoencoders for noise-resistant sample-wise fusion. To capture long-range dependencies, Liang et al. [1] extend pairwise connections to multi-order graphs through matrix exponentiation and preserve complex local structures through interactions among views, clusters, and graph orders.

Despite these advances, most graph-based methods remain restricted to pairwise topological formulations and, therefore, cannot propagate the high-order geometric structures needed for robust prealignment of heterogeneous geophysical sequences.

3.2. Subspace-Based Multi-View Clustering

Subspace-based methods assume that high-dimensional data can be represented by low-dimensional linear subspaces and seek to learn view-specific self-representation matrices [30,31]. Research in this area has focused primarily on improving representation quality and flexibility. Li et al. [32], for example, use orthogonal projection learning to map data jointly into a lower-dimensional space before tensor construction. To accommodate complex data distributions and limited sample sizes, researchers have also explored data-driven and nonlinear extensions. Ding et al. [33] alleviate the limitations associated with small sample sizes by using a data-driven Transformed Tensor Nuclear Norm (TTNN). Xu et al. [34] avoid predefined kernel functions by adopting a Data-Driven Kernel Learning Model (DKLM) to capture nonlinear manifolds.

However, these robust subspace techniques generally mitigate noise using element-wise sparse regularizers, such as the ℓ_1-norm. Because they treat anomalies as statistically independent events, they cannot adequately model and isolate the synchronous cross-view measurement errors commonly encountered in multi-tool downhole logging.

3.3. Deep Learning-Based Multi-View Clustering

Deep learning frameworks have advanced MVC because of their ability to model highly nonlinear data distributions [35,36]. A major focus in this area is the joint optimization of cross-view feature extraction and representation alignment. To balance view-specific contributions adaptively, Zhang et al. [37] use a mixture-of-experts (MoE)

architecture guided by a dynamic gating network. Contrastive learning has also become an important mechanism for structural alignment. Xiao et al. [38] improve the stability of view-level selection through optimal transport, whereas Cui et al. [39] improve intracluster compactness by dynamically redefining positive sample pairs using structure-guided nearest-neighbor graphs.

Although deep MVC models perform well on large-scale unstructured datasets, they typically require substantial amounts of training data. This requirement limits their applicability to geophysical exploration, where labeled or reliably aligned samples are often scarce.

4. Methodology

This section describes the proposed framework. We first present its motivation and three core modules. We then integrate these modules into a unified objective and introduce an ADMM-based optimization algorithm, followed by a computational complexity analysis.

4.1. Motivation

In lithofacies characterization, well-log data are inherently multimodal. Traditional multi-view clustering methods rely primarily on pairwise graphs, which cannot fully capture high-order semantic correlations among heterogeneous representations. Moreover, conventional methods treat measurement anomalies as independent pointwise noise within individual views. Consequently, they overlook the physical correlations among synchronous cross-view errors. Based on these observations, we design a three-stage pipeline that first prealigns the views using a shared hypergraph manifold, then separates concurrent anomalies through an explicit joint-group-sparse error matrix, and finally extracts a clean low-frequency tensor consensus.

4.2. Source-View Hypergraph Topology Injection

Consider a multi-view dataset with V views. Let $\boldsymbol{X}^v \in \mathbb{R}^{d_v \times N}$ denote the feature matrix of view v, where d_v is its feature dimension and N is the number of samples. In multi-view well-log analysis, heterogeneous measurement sequences are commonly organized around a primary reference tool, which we designate as the first view. We use the primary view as the topological source because auxiliary well-log views are typically derived from it, making it a representative physical reference for macroscopic geological structures. Its shared topology provides a common semantic anchor, as validated in Section Impact of Source View Selection.

To exploit this structural representativeness, we introduce a hypergraph topology-injection mechanism that models high-order semantic correlations in the primary well-log view rather than only pairwise relationships. Specifically, let $\mathcal{G}_{HG} = (\mathcal{V}, \mathcal{E}, \boldsymbol{W}_{\mathcal{E}})$ denote the hypergraph constructed from the source view $\boldsymbol{X}^1$, where $\mathcal{V}$ and $\mathcal{E}$ are the vertex and hyperedge sets, respectively. Each sample $i \in \mathcal{V}$ and its k nearest neighbors jointly form one hyperedge e_i, where k denotes the neighborhood size used for hypergraph construction. Thus, the number of hyperedges is $N_e = |\mathcal{E}| = N$.

The incidence matrix is denoted by $\boldsymbol{R} \in \mathbb{R}^{N \times N_e}$, where $R_{ie} = 1$ if vertex i belongs to hyperedge e, and $R_{ie} = 0$ otherwise. The hyperedge-weight matrix $\boldsymbol{W}_{\mathcal{E}} \in \mathbb{R}^{N_e \times N_e}$ is empirically set to $\boldsymbol{I}_{N_e}$ to represent uniform hyperedge confidence. The degrees of hyperedge e and vertex i are defined as

$$\delta(e) = \sum_{i=1}^{N} R_{ie}, \qquad d(i) = \sum_{e \in \mathcal{E}} R_{ie} (\boldsymbol{W}_{\mathcal{E}})_{ee}. \tag{1}$$

Accordingly, $\boldsymbol{D}_{\mathcal{V}} \in \mathbb{R}^{N \times N}$ and $\boldsymbol{D}_{\mathcal{E}} \in \mathbb{R}^{N_e \times N_e}$ denote the vertex- and hyperedge-degree matrices, respectively. The normalized hypergraph Laplacian is

$$\boldsymbol{L}_{HG} = \boldsymbol{I}_N - \boldsymbol{D}_{\mathcal{V}}^{-\frac{1}{2}} \boldsymbol{R} \boldsymbol{W}_{\mathcal{E}} \boldsymbol{D}_{\mathcal{E}}^{-1} \boldsymbol{R}^\top \boldsymbol{D}_{\mathcal{V}}^{-\frac{1}{2}}. \tag{2}$$

To propagate this reliable high-order structural prior to all heterogeneous views, we formulate a graph-signal-smoothing problem. Its objective is to obtain a smoothed representation $\tilde{\boldsymbol{X}}^v$ that preserves the original node features while penalizing variation over the hypergraph manifold. For each view v, we minimize the following energy function:

$$\min_{\tilde{\boldsymbol{X}}^v} \mathcal{J}(\tilde{\boldsymbol{X}}^v) = \|\tilde{\boldsymbol{X}}^v - \boldsymbol{X}^v\|_F^2 + \eta \, \mathrm{Tr}(\tilde{\boldsymbol{X}}^v \boldsymbol{L}_{HG} (\tilde{\boldsymbol{X}}^v)^\top), \tag{3}$$

where the first term enforces data fidelity, whereas the second term is the hypergraph Dirichlet energy that encourages structural consistency; η controls the strength of topology injection. Taking the first-order derivative of $\mathcal{J}$ with respect to $\tilde{\boldsymbol{X}}^v$ and setting it to zero yields

$$\frac{\partial \mathcal{J}}{\partial \tilde{\boldsymbol{X}}^v} = 2(\tilde{\boldsymbol{X}}^v - \boldsymbol{X}^v) + 2\eta \tilde{\boldsymbol{X}}^v \boldsymbol{L}_{HG} = \boldsymbol{0}. \tag{4}$$

Solving this equation gives the following closed-form solution:

$$\tilde{\boldsymbol{X}}^v = \boldsymbol{X}^v (\boldsymbol{I}_N + \eta \boldsymbol{L}_{HG})^{-1}. \tag{5}$$

This preprocessing step encourages all heterogeneous representations to follow the high-order geological manifold of the source view, thereby providing a geometrically aligned input for subsequent factorization.

4.3. Cross-View Concurrent Joint Group Sparsity

To obtain clean latent representations, we decompose the hypergraph-smoothed data $\tilde{\boldsymbol{X}}^v$ into a latent component and an explicit error matrix $\boldsymbol{E}^v \in \mathbb{R}^{d_v \times N}$. The reconstruction model is $\tilde{\boldsymbol{X}}^v = \boldsymbol{P}^v \boldsymbol{H}^v + \boldsymbol{E}^v$, where $\boldsymbol{P}^v \in \mathbb{R}^{d_v \times C}$ is a view-specific orthogonal basis matrix and $\boldsymbol{H}^v \in \mathbb{R}^{C \times N}$ is the corresponding latent representation.

To isolate localized measurement anomalies, we must account for their physical cross-view synchronicity in logging environments. We vertically concatenate the view-specific error matrices into the global cross-view error matrix $\boldsymbol{E}_{\text{cat}} = [(\boldsymbol{E}^1)^\top, \ldots, (\boldsymbol{E}^V)^\top]^\top$. Its i-th column, denoted by $\boldsymbol{e}_{\text{cat},i}$, represents the joint error vector of sample i across all V views.

By imposing the $\ell_{2,1}$-norm on $\boldsymbol{E}_{\text{cat}}$, where $\|\boldsymbol{E}_{\text{cat}}\|_{2,1} = \sum_{i=1}^N \|\boldsymbol{e}_{\text{cat},i}\|_2$, we enforce concurrent group sparsity. This regularizer encourages the errors associated with the same sample to be jointly retained or suppressed across all views, thereby capturing concurrent tool failures. Integrating this error-separation mechanism with the reconstruction model gives

$$\begin{aligned} \min_{\{\boldsymbol{P}^v, \boldsymbol{H}^v, \boldsymbol{E}^v\}_{v=1}^V} \quad & \sum_{v=1}^V \|\tilde{\boldsymbol{X}}^v - \boldsymbol{P}^v \boldsymbol{H}^v - \boldsymbol{E}^v\|_F^2 + \lambda \|\boldsymbol{E}_{\text{cat}}\|_{2,1} \\ \text{s.t.} \quad & (\boldsymbol{P}^v)^\top \boldsymbol{P}^v = \boldsymbol{I}_C, \qquad v = 1, \ldots, V. \end{aligned} \tag{6}$$

Here, λ is a trade-off parameter. The orthogonality constraint $(\boldsymbol{P}^v)^\top \boldsymbol{P}^v = \boldsymbol{I}_C$ prevents scale ambiguity during factorization and preserves the geometric metric in the learned representation $\boldsymbol{H}^v$.

4.4. Global Consensus via Smooth Tensor Nuclear Norm

In addition to isolating sample-specific anomalies, obtaining a coherent global representation requires modeling high-order correlations across views. We, therefore, construct a third-order tensor $\boldsymbol{\mathcal{H}} \in \mathbb{R}^{C \times V \times N}$ by stacking the latent representations $\boldsymbol{H}^v$ along the second mode:

$$\mathcal{H}_{\ell vi} = H^v_{\ell i}, \qquad \ell = 1, \ldots, C, \quad v = 1, \ldots, V, \quad i = 1, \ldots, N. \tag{7}$$

Equivalently, $\boldsymbol{\mathcal{H}} = \Phi(\boldsymbol{H}^1, \ldots, \boldsymbol{H}^V)$, where $\Phi(\cdot)$ denotes this mode-2 stacking operator.

The view and sample dimensions occupy the second and third modes, respectively. This arrangement allows the tensor singular value decomposition (t-SVD), which applies a one-dimensional Discrete Fourier Transform (DFT) along the third mode, to perform spectral operations along the ordered sample dimension.

With the tensor arranged in this form, we employ the Smooth Tensor Nuclear Norm (STNN) to regularize $\boldsymbol{\mathcal{H}}$. Let $\hat{\boldsymbol{\mathcal{H}}} = \mathcal{F}_3(\boldsymbol{\mathcal{H}})$ denote the mode-3 DFT of $\boldsymbol{\mathcal{H}}$. Following Long et al. [40], the STNN is defined as

$$\|\boldsymbol{\mathcal{H}}\|_{\mathrm{STNN}} = \|\hat{\boldsymbol{\mathcal{H}}}^{(1)}\|_* + \sum_{n=2}^{L} \left(\|\hat{\boldsymbol{\mathcal{H}}}^{(n)}\|_* + \|\hat{\boldsymbol{\mathcal{H}}}^{(N+2-n)}\|_* \right), \tag{8}$$

where $\hat{\boldsymbol{\mathcal{H}}}^{(n)}$ denotes the n-th frontal slice in the Fourier domain and L controls the retained low-frequency components. Due to the conjugate symmetry of the DFT for real-valued tensors, the paired slices $\hat{\boldsymbol{\mathcal{H}}}^{(n)}$ and $\hat{\boldsymbol{\mathcal{H}}}^{(N+2-n)}$ contain symmetric frequency information. By applying the nuclear norm to these low-frequency slices, the STNN simultaneously promotes smooth intra-view representations and captures the low-rank global correlations across different views.

From a geological perspective, the low-frequency components mainly characterize slowly varying and spatially continuous geological patterns, whereas high-frequency components are more sensitive to local fluctuations and measurement disturbances. Therefore, retaining and regularizing the low-frequency components enables the learned consensus representation to emphasize the dominant geological structures while reducing the influence of localized variations.

4.5. Overall Objective Formulation

By combining hypergraph topology injection, concurrent anomaly separation, and STNN-based consensus learning, we obtain the following unified objective:

$$\begin{aligned} \min_{\{\boldsymbol{P}^v, \boldsymbol{H}^v, \boldsymbol{E}^v\}_{v=1}^V, \boldsymbol{\mathcal{H}}} \quad & \sum_{v=1}^{V} \|\tilde{\boldsymbol{X}}^v - \boldsymbol{P}^v \boldsymbol{H}^v - \boldsymbol{E}^v\|_F^2 + \lambda \|\boldsymbol{E}_{\mathrm{cat}}\|_{2,1} + \gamma \|\boldsymbol{\mathcal{H}}\|_{\mathrm{STNN}} \\ \text{s.t.} \quad & (\boldsymbol{P}^v)^\top \boldsymbol{P}^v = \boldsymbol{I}_C, \qquad v = 1, \ldots, V, \\ & \boldsymbol{E}_{\mathrm{cat}} = [(\boldsymbol{E}^1)^\top, \ldots, (\boldsymbol{E}^V)^\top]^\top, \\ & \boldsymbol{\mathcal{H}} = \Phi(\boldsymbol{H}^1, \ldots, \boldsymbol{H}^V). \end{aligned} \tag{9}$$

Here, λ and γ are the joint-sparsity and STNN trade-off parameters, respectively, while η controls the preceding hypergraph smoothing step. The stacking operator $\Phi(\cdot)$ is defined elementwise above.

4.6. Optimization Algorithm

Because the objective contains multiple coupled variables, we use the Alternating Direction Method of Multipliers (ADMM) [41] for optimization. Introducing an auxiliary tensor $\boldsymbol{\mathcal{Z}}$ subject to $\boldsymbol{\mathcal{H}} = \boldsymbol{\mathcal{Z}}$ yields the following augmented Lagrangian:

$$\mathcal{L} = \sum_{v=1}^{V} \|\tilde{\boldsymbol{X}}^v - \boldsymbol{P}^v \boldsymbol{H}^v - \boldsymbol{E}^v\|_F^2 + \lambda \|\boldsymbol{E}_{\mathrm{cat}}\|_{2,1} + \gamma \|\boldsymbol{\mathcal{Z}}\|_{\mathrm{STNN}} + \langle \boldsymbol{\mathcal{W}}, \boldsymbol{\mathcal{H}} - \boldsymbol{\mathcal{Z}} \rangle + \frac{\mu}{2} \|\boldsymbol{\mathcal{H}} - \boldsymbol{\mathcal{Z}}\|_F^2, \tag{10}$$

where $\boldsymbol{\mathcal{W}}$ is the Lagrange multiplier tensor, $\mu > 0$ is the penalty parameter, and $\langle \cdot, \cdot \rangle$ denotes the Frobenius inner product between two tensors.

Update P^v: Fixing all other variables, the subproblem with respect to P^v is formulated as:

$$\max_{(P^v)^\top P^v = I_C} \mathrm{Tr}\left((P^v)^\top (\tilde{X}^v - E^v)(H^v)^\top\right), \tag{11}$$

Let $K^v = (\tilde{X}^v - E^v)(H^v)^\top$, and let its singular value decomposition (SVD) be $K^v = U^v \Sigma^v (V^v)^\top$. The globally optimal solution is

$$P^v = U^v (V^v)^\top. \tag{12}$$

Update H^v: Fixing all other variables, the subproblem with respect to H^v is formulated as:

$$\min_{H^v} \|\tilde{X}^v - E^v - P^v H^v\|_F^2 + \frac{\mu}{2}\left\|H^v - Z^v + \frac{W^v}{\mu}\right\|_F^2. \tag{13}$$

Taking the first-order derivative of this objective with respect to H^v and setting it to zero yields:

$$-2(P^v)^\top (\tilde{X}^v - E^v - P^v H^v) + \mu\left(H^v - Z^v + \frac{W^v}{\mu}\right) = \mathbf{0}. \tag{14}$$

Using the orthogonality constraint $(P^v)^\top P^v = I_C$, we obtain the following closed-form solution:

$$H^v = \frac{2(P^v)^\top (\tilde{X}^v - E^v) + \mu Z^v - W^v}{2 + \mu}. \tag{15}$$

Update E^v: Fixing all other variables, the optimization of the error matrices is decoupled into N column-wise subproblems:

$$\min_{\{E^v\}_{v=1}^V} \sum_{i=1}^{N}\left(\sum_{v=1}^{V} \|\tilde{x}_i^v - P^v h_i^v - e_i^v\|_2^2 + \lambda \|e_{\mathrm{cat},i}\|_2\right), \tag{16}$$

where $e_{\mathrm{cat},i} = [(e_i^1)^\top, \ldots, (e_i^V)^\top]^\top \in \mathbb{R}^{\sum_{v=1}^V d_v}$ is the i-th column of E_{cat}. Thus, the $\ell_{2,1}$-norm treats the errors associated with the same sample across all views as one group.

Let $a_i^v = \tilde{x}_i^v - P^v h_i^v \in \mathbb{R}^{d_v}$. Define the concatenated residual as

$$a_{\mathrm{cat},i} = [(a_i^1)^\top, \ldots, (a_i^V)^\top]^\top. \tag{17}$$

The subproblem for sample i is

$$\min_{e_{\mathrm{cat},i}} \frac{\lambda}{2}\|e_{\mathrm{cat},i}\|_2 + \frac{1}{2}\|e_{\mathrm{cat},i} - a_{\mathrm{cat},i}\|_2^2. \tag{18}$$

This subproblem has the block soft-thresholding solution stated in Lemma 1.

Lemma 1. *Given a vector a and a positive scalar $\tau > 0$, the minimizer of the following problem is obtained by block soft-thresholding [42]:*

$$\min_e \frac{1}{2}\|e - a\|_2^2 + \tau\|e\|_2 \tag{19}$$

Specifically, the solution is

$$e^\star = \begin{cases} \dfrac{\|a\|_2 - \tau}{\|a\|_2} a, & \text{if } \|a\|_2 > \tau; \\ \mathbf{0}, & \text{otherwise.} \end{cases} \tag{20}$$

By substituting $\boldsymbol{a} = \boldsymbol{a}_{\text{cat},i}$ and $\tau = \lambda/2$ into Lemma 1, the exact minimizer of (18) is

$$\boldsymbol{e}^{\star}_{\text{cat},i} = \max\left(1 - \frac{\lambda}{2\|\boldsymbol{a}_{\text{cat},i}\|_2}, 0\right)\boldsymbol{a}_{\text{cat},i}. \tag{21}$$

Update $\mathcal{Z}$: Fixing all other variables, the subproblem with respect to $\mathcal{Z}$ is formulated as

$$\min_{\mathcal{Z}} \quad \frac{\gamma}{\mu}\|\mathcal{Z}\|_{\text{STNN}} + \frac{1}{2}\left\|\mathcal{Z} - \left(\mathcal{H} + \frac{\mathcal{W}}{\mu}\right)\right\|_F^2. \tag{22}$$

This subproblem can be solved efficiently using a one-dimensional Discrete Fourier Transform (DFT) and Singular Value Thresholding (SVT). Let $\mathcal{T} = \mathcal{H} + \mathcal{W}/\mu$ and $\tau = \gamma/\mu$. Following the STNN strategy of Long et al. [40], the update of $\mathcal{Z}$ is summarized in Algorithm 1.

Algorithm 1 Solving the STNN Subproblem for $\mathcal{Z}$

Require: $\mathcal{H}$, $\mathcal{W}$, μ, γ, and L
$\mathcal{T} \leftarrow \mathcal{H} + \frac{\mathcal{W}}{\mu}$
$\tau \leftarrow \frac{\gamma}{\mu}$
$\hat{\mathcal{T}} \leftarrow \text{fft}(\mathcal{T}, [], 3)$
$\hat{\mathcal{Z}}^{(1)} \leftarrow \text{SVT}_\tau\left(\hat{\mathcal{T}}^{(1)}\right)$
for $n = 2$ **to** L **do**
    $\hat{\mathcal{Z}}^{(n)} \leftarrow \text{SVT}_\tau\left(\hat{\mathcal{T}}^{(n)}\right)$
    $\hat{\mathcal{Z}}^{(N+2-n)} \leftarrow \text{conj}\left(\hat{\mathcal{Z}}^{(n)}\right)$ /* conj$(\cdot)$ denotes element-wise complex conjugation */
end for
$\mathcal{Z} \leftarrow \text{ifft}(\hat{\mathcal{Z}}, [], 3)$
return $\mathcal{Z}$

Remark 1. ***(Mathematical validity of the STNN optimization).*** *Algorithm 1 follows the STNN optimization strategy of Long et al. [40]. Its mathematical validity can be understood from the proximal property of the matrix nuclear norm.*

Let $\mathcal{T} = \mathcal{H} + \frac{\mathcal{W}}{\mu}, \tau = \frac{\gamma}{\mu}$. According to the definition of the STNN, the low-rank regularization is applied to the retained low-frequency frontal slices in the Fourier domain. Therefore, for each retained slice, the corresponding matrix subproblem takes the form

$$\min_{\hat{\mathcal{Z}}^{(n)}} \tau\left\|\hat{\mathcal{Z}}^{(n)}\right\|_* + \frac{1}{2}\left\|\hat{\mathcal{Z}}^{(n)} - \hat{\mathcal{T}}^{(n)}\right\|_F^2. \tag{23}$$

Let $\hat{\mathcal{T}}^{(n)} = \boldsymbol{U}_n\boldsymbol{\Sigma}_n\boldsymbol{V}_n^H$ be the singular value decomposition of the n-th Fourier slice. Problem (23) is the standard proximal problem of the matrix nuclear norm, whose closed-form solution is given by the singular value thresholding (SVT) operator:

$$\hat{\mathcal{Z}}^{(n)} = \text{SVT}_\tau\left(\hat{\mathcal{T}}^{(n)}\right) = \boldsymbol{U}_n(\boldsymbol{\Sigma}_n - \tau\boldsymbol{I})_+\boldsymbol{V}_n^H. \tag{24}$$

Here, $(\cdot)_+$ denotes soft-thresholding of the singular values.

Moreover, because the input tensor is real-valued, its Fourier coefficients satisfy conjugate symmetry. Hence, the symmetric frequency slices can be directly recovered as

$$\hat{\mathcal{Z}}^{(N+2-n)} = \text{conj}\left(\hat{\mathcal{Z}}^{(n)}\right), \qquad n = 2, \ldots, L, \tag{25}$$

which allows the corresponding symmetric frequency slices to be recovered directly and avoids redundant SVD computations. Therefore, the slice-wise SVT operation adopted in Algorithm 1 has a well-defined closed-form solution for each retained low-frequency STNN component, providing the mathematical basis for the adopted STNN optimization.

Update Multipliers and Penalty:

$$\boldsymbol{\mathcal{W}} = \boldsymbol{\mathcal{W}} + \mu(\boldsymbol{\mathcal{H}} - \boldsymbol{\mathcal{Z}}). \tag{26}$$

$$\mu = \min(\rho\mu, \mu_{\max}). \tag{27}$$

Here, $\rho > 1$ increases the penalty parameter to accelerate convergence, and $\mu_{\max}$ is its predefined upper bound.

The solution procedure of the proposed model is summarized in Algorithm 2. To facilitate independent verification and reproducibility, the source code and experimental implementation are publicly available at https://anonymous.4open.science/status/HTCGS-344C, accessed on 23 September 2026.

Algorithm 2 Optimization Algorithm for the Proposed Framework

Require: Multi-view well-log data $\{\boldsymbol{X}^v\}_{v=1}^V$, number of clusters C, trade-off parameters η, λ, γ, and low-frequency cutoff L

/* Data Preprocessing */
Set the normalization safeguard $\varepsilon_0 \leftarrow 10^{-7}$
for $v = 1$ **to** V **do**
    $\boldsymbol{x}_i^v \leftarrow \boldsymbol{x}_i^v / \max(\|\boldsymbol{x}_i^v\|_2, \varepsilon_0), i = 1, \ldots, N$
end for
/* Phase 1: Source-View Hypergraph Topology Injection */
Set the neighborhood size $k \leftarrow 5$
Construct $\boldsymbol{R}$ and $\boldsymbol{W}_{\mathcal{E}}$ from the source view $\boldsymbol{X}^1$ using k-nearest-neighbor hyperedges
Compute the normalized hypergraph Laplacian matrix via Equation (2)
for $v = 1$ **to** V **do**
    Extract the hypergraph-smoothed representation via Equation (5)
end for
/* Phase 2: ADMM Initialization */
Initialize each $\boldsymbol{P}^v$ with orthonormal columns and set $\boldsymbol{H}^v, \boldsymbol{E}^v \leftarrow \boldsymbol{0}$
Initialize $\boldsymbol{\mathcal{Z}}, \boldsymbol{\mathcal{W}} \leftarrow \boldsymbol{0}$ and $\mu \leftarrow 0.01$
Set $T_{\max} \leftarrow 150$, $\xi \leftarrow 10^{-6}$, $\mu_{\max} \leftarrow 10^8$, and $\rho \leftarrow 1.5$
/* Phase 3: Iterative Optimization */
for $r = 1$ **to** $T_{\max}$ **do**
    1. Update View-Specific Variables and Errors
    for $v = 1$ **to** V **do**
        Update $\boldsymbol{P}^v$ via Equation (12)
        Update $\boldsymbol{H}^v$ via Equation (15)
    end for
    Update $\boldsymbol{e}_{\text{cat},i}$ by block soft-thresholding and recover $\{\boldsymbol{E}^v\}_{v=1}^V$ via Equation (21)
    2. Update Global Tensor Regularization
    Construct tensor $\boldsymbol{\mathcal{H}} \in \mathbb{R}^{C \times V \times N}$ by stacking $\{\boldsymbol{H}^v\}_{v=1}^V$
    Update $\boldsymbol{\mathcal{Z}}$ via Algorithm 1
    3. Update Multipliers and Penalty
    Update $\boldsymbol{\mathcal{W}}$ via Equation (26)
    Update μ via Equation (27)
    4. Check Convergence
    if $\max_{1 \le v \le V} \|\boldsymbol{H}^v - \boldsymbol{Z}^v\|_\infty < \xi$ **then**
        break
    end if
end for
$\boldsymbol{Z}_{\text{con}} \leftarrow \frac{1}{V} \sum_{v=1}^V \boldsymbol{Z}^v$
Return clustering labels obtained by applying K-means to $\boldsymbol{Z}_{\text{con}}$.

Because the view-specific representations $\{\boldsymbol{Z}^v\}_{v=1}^V$ lie in the same latent space and are jointly regularized by the STNN, equal averaging provides a parameter-free and symmetric way to extract their common information. This widely used multi-view clustering strategy also avoids the dimensional expansion and view-specific redundancy introduced by direct concatenation.

4.7. Computational Complexity Analysis

Let N, V, C, $d = \max_v d_v$, and $T_{\max}$ denote the number of samples, number of views, number of clusters, maximum feature dimension, and maximum number of ADMM iterations, respectively. The overall complexity consists of a one-time preprocessing phase and an iterative optimization stage. The one-time preprocessing stage, which comprises hypergraph construction and signal smoothing, has a complexity of $\mathcal{O}(N^3 + VN^2d)$. Although this cost is cubic in N, the stage is executed only once. During each iteration, the complexities of updating $\boldsymbol{P}^v$, $\boldsymbol{H}^v$, and $\boldsymbol{E}^v$ are $\mathcal{O}(V(NCd + dC^2))$, $\mathcal{O}(VNCd)$, and $\mathcal{O}(VNd)$, respectively. Updating the STNN tensor through a DFT and SVDs of the retained low-frequency slices requires $\mathcal{O}(CVN \log N + LCV^2)$ operations. Because C, V, and L are typically much smaller than N, the per-iteration complexity is dominated by $\mathcal{O}(VNCd + CVN \log N)$, which is approximately linear in the number of samples when C, V, L, and d are fixed. Therefore, the total computational complexity is approximately $\mathcal{O}(N^3 + VN^2d + T_{\max}(VNCd + CVN \log N))$.

5. Experiments

5.1. Datasets

We evaluate the proposed framework on five real-world geophysical datasets: **Volcanic** (https://data.mendeley.com/datasets/dsv68j6jg2/1, accessed on 23 September 2026.), **Facies** (https://github.com/mardani72/Facies-Classification-Machine-Learning/tree/master, accessed on 23 September 2026.), **35-6-2-S-well**, **25-5-3-well** (https://www.kaggle.com/datasets/faresazzam/well-logs-dataset-for-machine-learning, accessed on 23 September 2026.), and **cigFacies** [43]. These benchmarks cover diverse geological structures and multimodal feature representations. The dataset statistics are shown in Table 2, and their configurations are summarized below:

- **Volcanic**: This dataset characterizes complex nonlinear lithofacies in the Kebai Fault Zone. It comprises three views: five original well-log responses, four derived petrophysical parameters, and ten rolling-window texture descriptors.
- **Facies**: This dataset, obtained from the Hugoton and Panoma fields in North America, captures vertical stratigraphic transitions. It contains two views: seven petrophysical attributes and 18 depthwise spatial-context features.
- **35-6-2-S-well** and **25-5-3-well**: Derived from the FORCE 2020 North Sea offshore exploration data, these datasets contain sequential well logs with concurrent downhole anomalies, such as washouts. Both are partitioned into three views using the same scheme: 16 primary well-log features, six interface-gradient features, and 12 spatial-statistical features.
- **cigFacies**: This large-scale seismic benchmark has substantial dimensional asymmetry across its two views. It combines a 16,384-dimensional raw seismic-pixel view with a compact 12-dimensional morphological-feature view.

5.2. Baseline Models

We compare the proposed framework with six recent representative multi-view clustering methods. These baselines are selected to cover complementary methodological directions, including reliable anchor construction, tensorized anchor-graph learning, nonconvex low-rank subspace learning, direct shared-embedding clustering, robust consensus anchor graphs, and joint graph construction with spectral decomposition. We also consider publication recency, availability of the original implementation, and compatibility with the evaluated multi-view datasets. Accordingly, the selected methods provide broad and technically diverse comparisons. These models are described as follows:

- **LASD** (ACMMM'25) [44]: This method uses optimal transport to construct structurally reliable anchors that preserve the geometric distribution of the original data.
- **TMC** (TKDE'26) [45]: This method stacks view-specific anchor graphs into a tensor and uses multi-rank regularization to enforce an explicit block-diagonal structure.
- **NLRSC** (IJCAI'24) [46]: This subspace method uses a nonconvex penalty to recover global low-rank structure while reducing the adverse effects of corrupted or isolated samples.
- **OMVCDR** (TNNLS'25) [47]: This unified method maps heterogeneous features into a shared embedding space and directly produces the final cluster assignments, thereby avoiding a conventional two-stage procedure.
- **RCAGL** (TKDE'24) [48]: This method constructs a robust consensus anchor graph by separating shared topological consistency from view-specific discrepancies.
- **NSEAN** (NN'26) [49]: This framework integrates dynamic graph construction with nonnegative spectral decomposition to reduce the error accumulation associated with separate processing stages.

5.3. Evaluation Metrics and Experimental Settings

We use six widely adopted metrics to evaluate the clustering performance of the proposed method and the baselines: accuracy (ACC), normalized mutual information (NMI), purity, F-score, precision, and adjusted Rand index (ARI). All values are reported as percentages (%), and higher values indicate better performance.

All experiments are conducted on a desktop workstation equipped with a 12th-generation Intel Core i5-12600K CPU and 32 GB of RAM. HTCGS and most baseline methods are run in MATLAB R2022b, whereas NSEAN is run in Python 3.8.

To ensure a fair comparison, the hyperparameters of each baseline are tuned by grid search over the ranges recommended in its original publication. For HTCGS, the trade-off parameters η, λ, and γ are selected from $\{10^{-4}, 5\times10^{-4}, 10^{-3}, 5\times10^{-3}, 10^{-2}, 5\times10^{-2}, 10^{-1}, 5\times10^{-1}, 1, 5, 10, 50, 100\}$, and L is selected from $\{10, 20, 30\}$. Each experiment is repeated independently ten times, and all results are reported as the mean $\pm$ standard deviation. The parameter settings used for every method on each dataset are summarized in Table 3.

Table 2. Statistics of the benchmark datasets.

Benchmark Dataset	Samples (N)	Views (V)	Clusters (C)	Feature Dimensions (d_v)
Volcanic	747	3	5	[5, 4, 10]
Facies	3232	2	9	[7, 18]
35-6-2-S-well	13,075	3	7	[16, 6, 12]
25-5-3-well	856	3	5	[16, 6, 12]
cigFacies	8001	2	5	[16,384, 12]

Table 3. Parameter settings used by all evaluated models on the different datasets. Here, c denotes the number of clusters, and "–" indicates that no valid clustering result was obtained.

Model	Parameters	Volcanic	Facies	35-6-2-S-well	25-5-3-well	cigFacies
LASD	η	10^9	10^3	10^{11}	10^9	10^3
TMC	λ, k	10^{-1}, $5c$	10^{-1}, $2c$	10^{-2}, $5c$	10^{-1}, $2c$	10^{-3}, $5c$
NLRSC	λ, β	10^{-1}, 10^{-3}	10^{-3}, 10^{-2}	–	10^{-2}, 10^{-1}	–
OMVCDR	λ	1	2^{-5}	4	2^{-3}	2^{-3}
RCAGL	m, λ	$3c$, 10^2	$2c$, 10^2	c, 10^2	$2c$, 10^2	c, 10^3
NSEAN	k	20	20	20	20	20
Ours	λ, η, γ, L	5×10^{-2}, 10, 5, 10	5, 10^2, 10^2, 10	5×10^{-4}, 10^2, 5, 20	5×10^{-3}, 10^2, 5, 10	10^{-1}, 10^{-3}, 10, 10

5.4. Results and Discussion

Table 4 compares HTCGS with six recent representative baselines. The "NaN" entries for NLRSC on the 35-6-2-S-well and cigFacies datasets indicate that the method does not produce valid clustering results. During execution, its matrix-inversion operations result in numerical instability or singular matrices, and the associated memory demand prevents stable completion on these datasets. HTCGS achieves the best performance on all five datasets. For example, it obtains an ACC of 88.35% and an NMI of 81.13% on the Volcanic dataset. On 35-6-2-S-well, HTCGS outperforms TMC on every metric, with improvements of 11.80, 10.91, 4.55, 12.01, 10.71, and 14.45 percentage points in ACC, NMI, purity, F-score, precision, and ARI, respectively. HTCGS also maintains strong performance on the large-scale 35-6-2-S-well dataset ($N = 13{,}075$) and the high-dimensional cigFacies dataset ($d = 16{,}384$).

Table 4. Clustering performance comparison of different methods across five benchmark datasets. All results are reported as the mean ± standard deviation over ten independent runs. The best results are highlighted in **bold**.

Dataset	Method	ACC	NMI	Purity	F-Score	Precision	ARI
Volcanic	LASD	53.55 ± 0.00	30.67 ± 0.00	61.98 ± 0.00	43.91 ± 0.00	48.24 ± 0.00	27.69 ± 0.00
	TMC	55.02 ± 0.00	34.57 ± 0.00	63.99 ± 0.00	45.39 ± 0.00	49.99 ± 0.00	29.65 ± 0.00
	NLRSC	41.41 ± 0.06	19.64 ± 0.13	53.76 ± 0.12	34.53 ± 0.06	37.86 ± 0.04	15.56 ± 0.06
	OMVCDR	58.50 ± 0.00	31.86 ± 0.00	62.12 ± 0.00	48.06 ± 0.00	43.42 ± 0.00	28.58 ± 0.00
	RCAGL	50.28 ± 0.16	17.64 ± 0.34	50.41 ± 0.16	43.30 ± 0.05	33.96 ± 0.02	17.33 ± 0.00
	NSEAN	49.13 ± 0.00	27.39 ± 0.00	58.10 ± 0.00	41.44 ± 0.00	44.13 ± 0.00	23.99 ± 0.00
	Ours	**88.35 ± 0.28**	**81.13 ± 0.27**	**90.50 ± 0.21**	**85.54 ± 0.31**	**89.82 ± 0.26**	**81.11 ± 0.39**
Facies	LASD	39.88 ± 0.00	35.65 ± 0.00	47.18 ± 0.00	31.91 ± 0.00	33.61 ± 0.00	20.62 ± 0.00
	TMC	34.47 ± 0.00	25.94 ± 0.00	42.11 ± 0.00	25.86 ± 0.00	29.45 ± 0.00	14.63 ± 0.00
	NLRSC	34.41 ± 0.01	28.52 ± 0.02	42.41 ± 0.01	27.18 ± 0.01	31.40 ± 0.00	16.33 ± 0.01
	OMVCDR	41.89 ± 0.00	37.27 ± 0.00	43.90 ± 0.00	43.00 ± 0.00	35.41 ± 0.00	30.33 ± 0.00
	RCAGL	36.74 ± 1.08	30.42 ± 0.50	41.61 ± 0.12	33.30 ± 0.03	29.07 ± 0.09	19.48 ± 0.07
	NSEAN	34.23 ± 0.21	27.86 ± 0.04	42.45 ± 0.00	28.85 ± 0.01	30.18 ± 0.00	16.36 ± 0.00
	Ours	**79.38 ± 0.93**	**77.46 ± 0.49**	**81.58 ± 0.57**	**75.97 ± 0.81**	**71.31 ± 0.94**	**71.41 ± 0.97**
35-6-2-S-well	LASD	51.40 ± 0.00	45.84 ± 0.00	65.39 ± 0.00	43.51 ± 0.00	48.63 ± 0.00	29.62 ± 0.00
	TMC	63.99 ± 0.00	61.15 ± 0.00	81.56 ± 0.00	60.87 ± 0.00	71.56 ± 0.00	51.84 ± 0.00
	NLRSC	NaN	NaN	NaN	NaN	NaN	NaN
	OMVCDR	53.76 ± 0.00	48.74 ± 0.00	64.58 ± 0.00	53.50 ± 0.00	53.30 ± 0.00	40.28 ± 0.00
	RCAGL	59.63 ± 0.06	48.30 ± 0.16	66.15 ± 0.14	60.34 ± 0.28	61.25 ± 0.45	49.33 ± 0.39
	NSEAN	52.70 ± 0.00	38.61 ± 0.00	61.02 ± 0.00	47.77 ± 0.00	49.94 ± 0.00	33.07 ± 0.00
	Ours	**75.79 ± 0.01**	**72.06 ± 0.05**	**86.11 ± 0.00**	**72.88 ± 0.02**	**82.27 ± 0.12**	**66.29 ± 0.04**
25-5-3-well	LASD	63.43 ± 0.00	59.04 ± 0.00	77.92 ± 0.00	59.57 ± 0.00	66.63 ± 0.00	47.86 ± 0.00
	TMC	64.60 ± 0.00	59.80 ± 0.00	76.29 ± 0.00	61.65 ± 0.00	66.43 ± 0.00	50.00 ± 0.00
	NLRSC	61.92 ± 0.00	56.63 ± 0.00	70.21 ± 0.00	57.25 ± 0.00	59.93 ± 0.00	43.76 ± 0.00
	OMVCDR	52.22 ± 0.00	44.33 ± 0.00	59.81 ± 0.00	51.11 ± 0.00	44.76 ± 0.00	31.45 ± 0.00
	RCAGL	64.88 ± 0.11	57.19 ± 0.34	69.87 ± 0.16	57.69 ± 0.03	55.12 ± 0.30	42.61 ± 0.14
	NSEAN	52.10 ± 0.00	50.19 ± 0.00	68.93 ± 0.00	54.06 ± 0.00	59.51 ± 0.00	35.47 ± 0.00
	Ours	**87.58 ± 0.83**	**83.12 ± 0.70**	**91.17 ± 0.46**	**87.26 ± 0.72**	**88.23 ± 0.34**	**83.06 ± 0.92**

Table 4. *Cont.*

Dataset	Method	ACC	NMI	Purity	F-Score	Precision	ARI
cigFacies	LASD	54.91 ± 0.00	32.87 ± 0.00	54.91 ± 0.00	43.86 ± 0.00	44.17 ± 0.00	29.69 ± 0.00
	TMC	53.01 ± 0.00	30.37 ± 0.00	53.01 ± 0.00	43.53 ± 0.00	42.50 ± 0.00	28.71 ± 0.00
	NLRSC	NaN	NaN	NaN	NaN	NaN	NaN
	OMVCDR	40.94 ± 0.00	15.84 ± 0.00	40.98 ± 0.00	40.84 ± 0.00	28.12 ± 0.00	16.10 ± 0.00
	RCAGL	54.45 ± 0.01	31.16 ± 0.00	57.79 ± 0.02	45.72 ± 0.00	41.99 ± 0.01	30.32 ± 0.01
	NSEAN	52.10 ± 0.00	50.19 ± 0.00	68.93 ± 0.00	54.06 ± 0.00	59.51 ± 0.00	35.47 ± 0.00
	Ours	**86.32 ± 0.43**	**76.51 ± 0.40**	**86.33 ± 0.39**	**78.43 ± 0.34**	**76.73 ± 0.31**	**72.26 ± 1.99**

5.5. Comprehensive Multi-Metric Analysis

Figure 2 provides a comprehensive comparison of the six evaluation metrics across the five datasets. In general, HTCGS forms larger and more outwardly extended radar polygons than the competing methods, indicating that its advantages are consistently reflected across multiple evaluation criteria rather than being limited to a single metric. The relatively regular shapes of the HTCGS polygons also suggest a more balanced performance profile without obvious degradation in any particular aspect. In comparison, NLRSC fails to produce valid results on 35-6-2-S-well and cigFacies, while TMC and OMVCDR exhibit more uneven radar profiles on several datasets, indicating less consistent performance across different metrics. Overall, the radar-chart analysis further demonstrates that HTCGS achieves both strong clustering performance and favorable multi-metric consistency across datasets with different geological characteristics and feature configurations, supporting the effectiveness and robustness of the proposed multi-view fusion strategy.

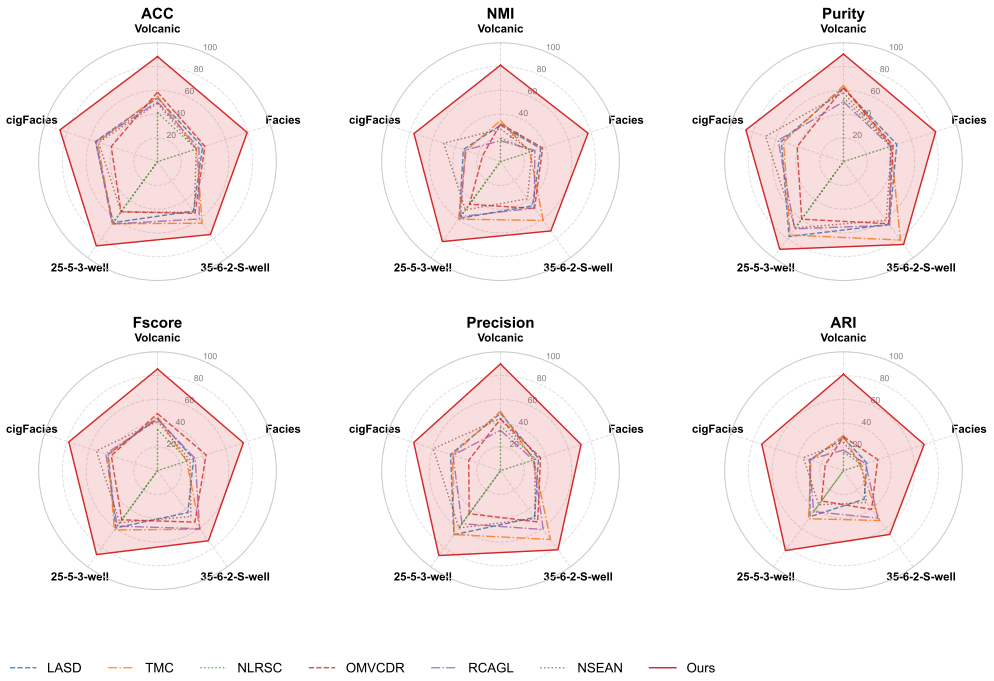


Figure 2. Radar charts comparing clustering performance on five benchmark datasets using six evaluation metrics.

5.6. Impact of Source View Selection

To evaluate the representativeness of the default source view (View 1) for hypergraph topology injection, we measure the changes in clustering performance when each available view is used as the reference on three datasets: Volcanic, Facies, and 25-5-3-well. As shown in Table 5, HTCGS consistently achieves its best performance with View 1. On the

Volcanic dataset, for example, View 1 yields an ACC of 88.35%, compared with 84.63% for View 2 and 63.11% for View 3. From a geophysical perspective, View 1 contains continuous primary petrophysical measurements and, therefore, provides a reliable high-order semantic anchor. Auxiliary views may contain localized environmental disturbances, such as borehole washouts; using such a view as the topological source can propagate structural artifacts across modalities and weaken the cross-view consensus.

Table 5. Clustering performance under different source-view selections for hypergraph construction. The best results are highlighted in **bold**.

Dataset	Source View	ACC	NMI	Purity	F-Score	Precision	ARI
Volcanic	View 1	**88.35**	**81.13**	**90.50**	**85.54**	**89.82**	**81.11**
	View 2	84.63	72.38	86.76	78.10	81.86	71.38
	View 3	63.11	57.20	79.97	64.23	70.45	53.87
Facies	View 1	**79.38**	**77.46**	**81.58**	**75.97**	**71.31**	**71.41**
	View 2	69.48	71.52	74.46	65.13	60.91	58.47
25-5-3-well	View 1	**87.58**	**83.12**	**91.17**	**87.26**	**88.23**	**83.06**
	View 2	62.30	56.65	67.73	60.21	65.70	48.31
	View 3	76.29	66.96	80.36	73.47	74.06	64.65

5.7. Parameter Sensitivity Analysis

We conduct a sensitivity analysis of the three trade-off parameters η, λ, and γ and the low-frequency cutoff L. As shown in Figures 3–6, clustering performance is evaluated on four benchmark datasets using $\eta, \lambda, \gamma \in \{10^{-4}, 10^{-3}, 10^{-2}, 10^{-1}, 10^{0}, 10^{1}, 10^{2}\}$ and $L \in \{10, 15, 20, 25, 30, 35, 40\}$.

The results show that HTCGS maintains relatively stable clustering performance over a broad range of parameter combinations. The parameters η, λ, and γ balance the contributions of hypergraph topology injection, concurrent group sparsity, and smooth tensor regularization, respectively, while L controls the range of frequencies retained by the low-pass tensor filter. HTCGS generally performs well for $\lambda \in [10^{-4}, 10^{-1}]$, $\eta \in [10^{0}, 10^{2}]$, $\gamma \in [10^{1}, 10^{2}]$, and $L \in [10, 20]$. These ranges provide practical guidance for parameter selection.

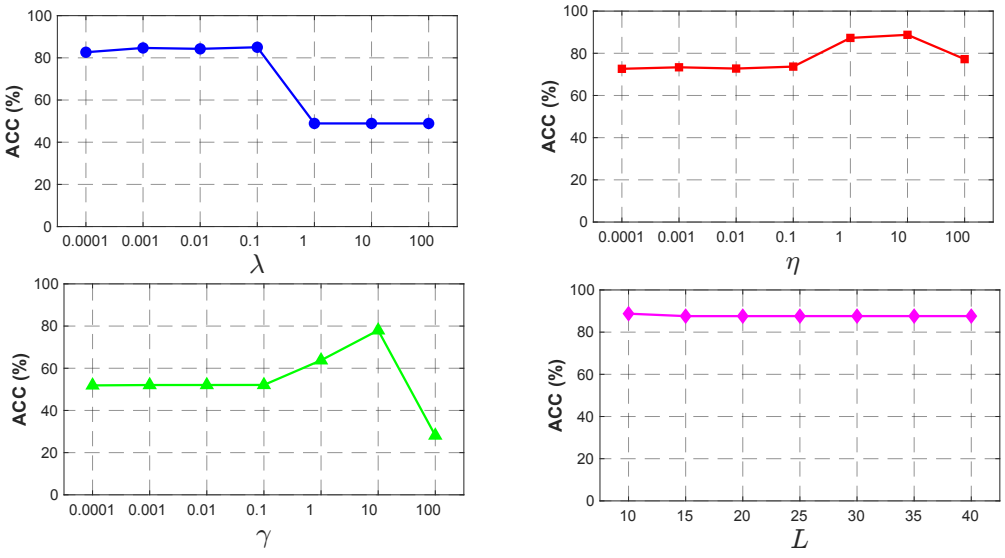


Figure 3. Parameter sensitivity of HTCGS on the Volcanic dataset.

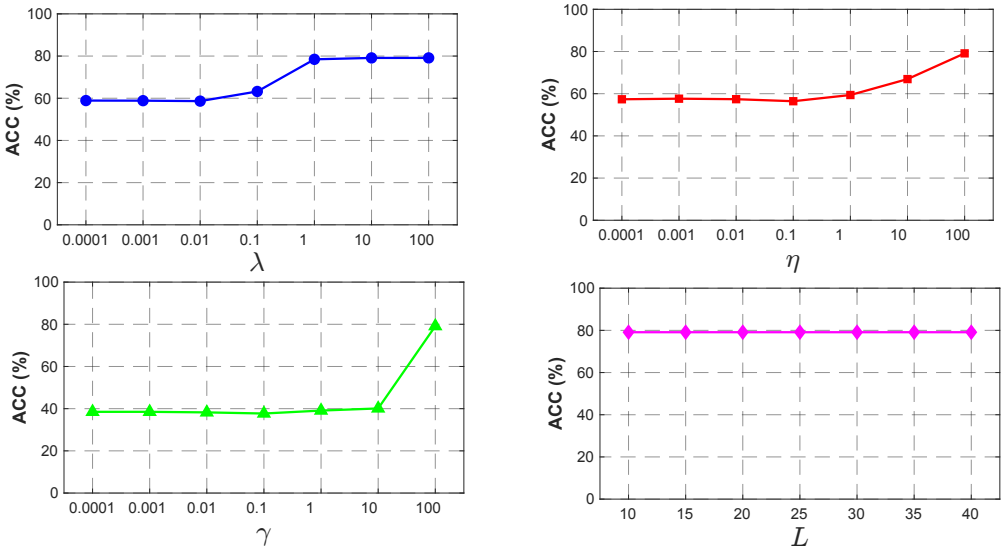


Figure 4. Parameter sensitivity of HTCGS on the Facies dataset.

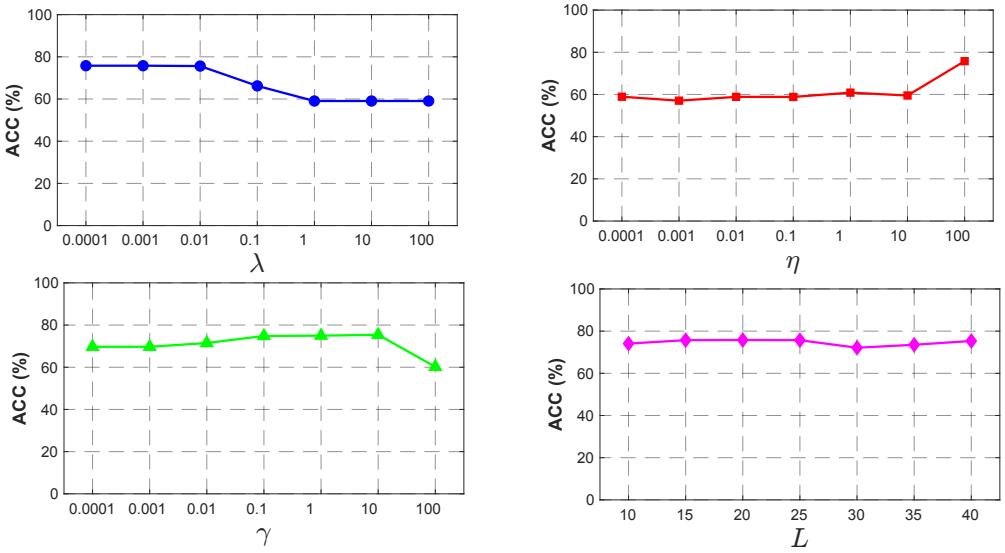


Figure 5. Parameter sensitivity of HTCGS on the 35-6-2-S-well dataset.

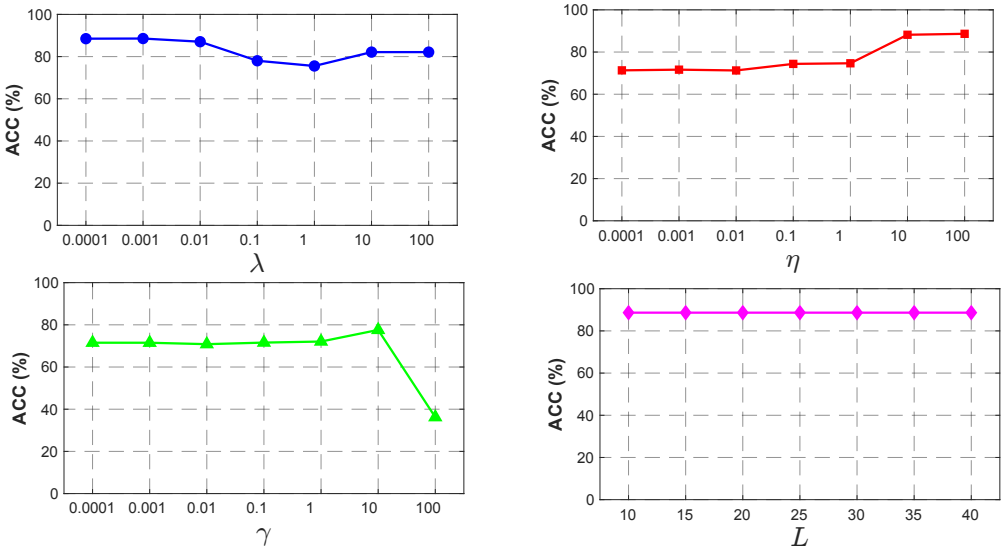


Figure 6. Parameter sensitivity of HTCGS on the 25-5-3-well dataset.

We also investigate the effect of the neighborhood size k, defined as the number of nearest neighbors, on source-view hypergraph construction. As shown in Figure 7, we evaluate $k \in \{3, 5, 7, 9, 11, 15, 20\}$. A value of k that is too small may provide insufficient topological context, whereas an excessively large value may introduce heterogeneous noise and oversmooth the manifold. The results indicate that HTCGS is generally robust to k and performs consistently when k lies in a moderate range, such as $[5, 11]$. Accordingly, k is fixed at 5 in all reported experiments rather than tuned separately for each dataset.

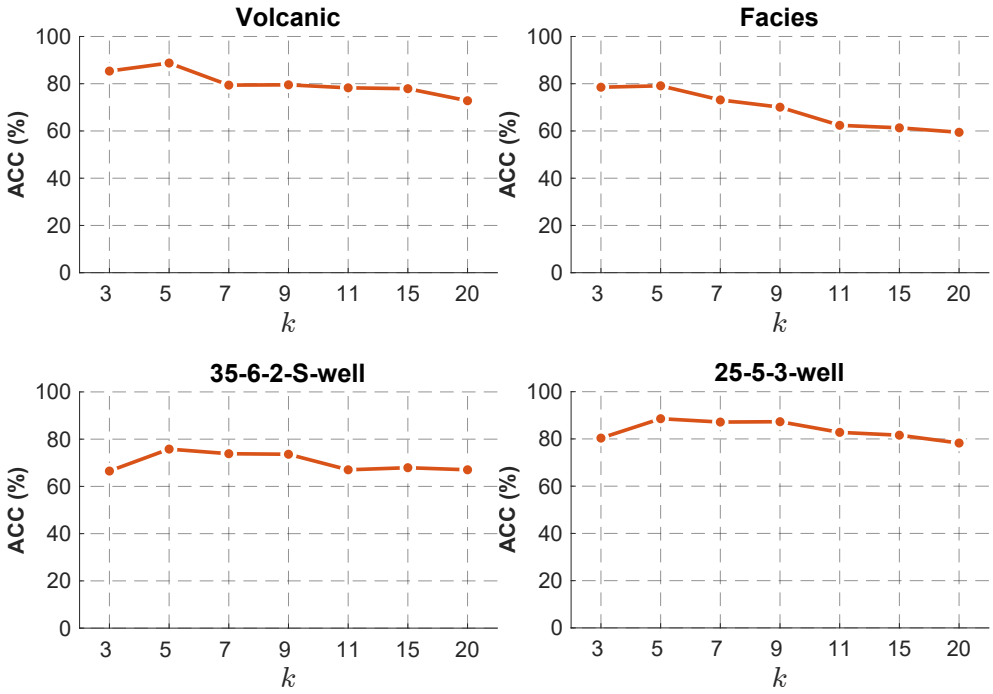


Figure 7. Sensitivity curves for the nearest-neighbor parameter k on the benchmark datasets.

5.8. Running Time Analysis

We record the runtime of each method on all five benchmark datasets using the same desktop workstation equipped with a 12th-generation Intel Core i5-12600K CPU and 32 GB of RAM. Figure 8 presents the runtime comparison using a $\log_{10}(\text{Time} + 1)$ scale to accommodate the substantial differences among methods and datasets. HTCGS achieves the lowest runtime on Volcanic, Facies, and 25-5-3-well, and remains computationally competitive on 35-6-2-S-well. On the large-scale cigFacies dataset, HTCGS does not show a clear runtime advantage because the method involves a one-time cubic operation with respect to the number of samples, which becomes increasingly expensive as the dataset size grows. Since this operation is performed only once before the iterative optimization, the increased runtime on cigFacies mainly reflects the preprocessing overhead rather than the cost of the subsequent optimization iterations. The missing NLRSC results on 35-6-2-S-well and cigFacies correspond to failed executions rather than zero runtime. Overall, HTCGS maintains favorable computational efficiency on most datasets while remaining computationally feasible on the largest benchmark.

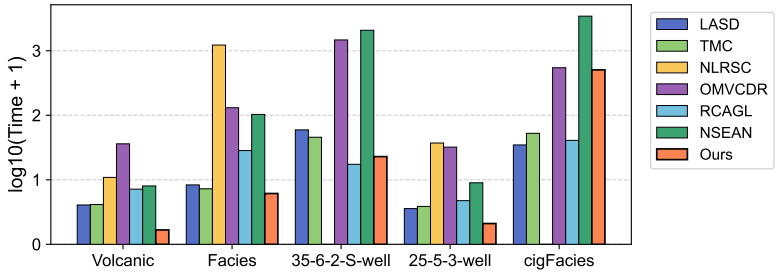


Figure 8. Runtime comparison of the multi-view clustering methods on five benchmark datasets. Runtime is measured in seconds and displayed on a $\log_{10}(\text{Time}+1)$ scale.

5.9. Memory Consumption Comparison

We further compare the memory consumption of the evaluated methods on the five benchmark datasets. As shown in Figure 9, memory usage is measured in megabytes (MB) and displayed on a $\log_{10}(\text{Memory}+1)$ scale to accommodate the substantial differences among methods and datasets. Across the four well-log datasets, HTCGS maintains modest and generally competitive memory consumption without exhibiting the extreme memory demand observed for some baselines. Its memory consumption increases on the cigFacies dataset because of the additional storage required to process the extremely high-dimensional raw seismic view, indicating that input dimensionality remains a major memory bottleneck in this setting. The missing bars for NLRSC on 35-6-2-S-well and cigFacies correspond to failed executions. Overall, the comparison shows that HTCGS has practical memory requirements on the well-log datasets, while further memory optimization remains desirable for extremely high-dimensional seismic data.

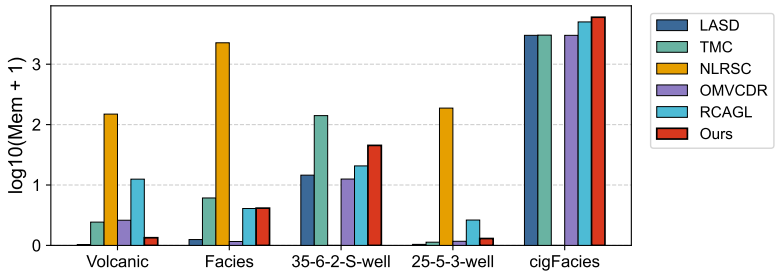


Figure 9. Memory consumption comparison of the MATLAB-based multi-view clustering methods on five benchmark datasets. Memory usage is measured in megabytes and displayed on a $\log_{10}(\text{Memory}+1)$ scale. NSEAN is excluded because it is implemented in Python 3.8, and its memory usage is, therefore, not directly comparable with that of the MATLAB-based methods.

5.10. Convergence Analysis

To assess the convergence behavior of the proposed optimization algorithm, we monitor the maximum infinity-norm residual between the latent representations and their corresponding auxiliary variables, defined as $\max_{1\le v\le V}\|\boldsymbol{H}^v-\boldsymbol{Z}^v\|_\infty$. This residual reflects the degree to which the equality constraints are satisfied during the iterative optimization process, and a smaller value indicates that the latent representations and auxiliary variables become increasingly consistent. As shown in Figure 10, the maximum residual decreases rapidly during the early iterations and then gradually approaches a stable level. The algorithm converges within approximately 30–50 iterations on all five datasets, despite the differences in sample size, feature dimensionality, and data characteristics. These results indicate that the proposed optimization procedure exhibits fast and stable empirical convergence across different geological datasets.

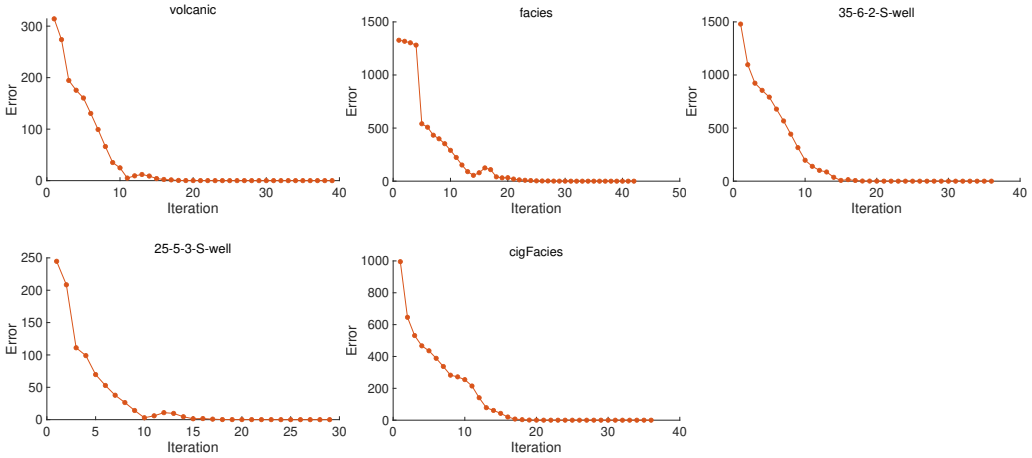


Figure 10. Convergence curves of the proposed HTCGS framework on the five benchmark datasets, illustrating the monotonic decrease of the maximum infinity-norm residual.

5.11. Ablation Study

To examine the contribution of each core component of HTCGS, we evaluate the following four ablated variants:

- **Variant-I (w/o HTI):** Disables Hypergraph Topology Injection and uses the original feature representations.
- **Variant-II (w/o CGS):** Removes the Concurrent Group Sparsity regularizer based on the $\ell_{2,1}$-norm.
- **Variant-III (w/o STNN):** Replaces the Smooth Tensor Nuclear Norm with the standard tensor nuclear norm.
- **Variant-IV (Single View):** Uses only the first well-log view.

Table 6 reports the performance of HTCGS and its variants. Replacing the STNN with the standard tensor nuclear norm (**Variant-III**) substantially reduces performance, demonstrating the importance of sample-wise low-pass filtering for suppressing high-frequency noise while preserving macroscopic geological continuity. Removing Concurrent Group Sparsity (**Variant-II**) also degrades performance on most datasets, showing that the $\ell_{2,1}$-norm helps isolate concurrent multi-tool errors and preserve the latent representations. In addition, **Variant-I (w/o HTI)** generally underperforms the full model, which supports the use of hypergraph topology for prealigning heterogeneous features. Finally, the single-view model (**Variant-IV**) performs worse than the full model on all datasets. Together, these results demonstrate the complementary contributions of the principal design choices in HTCGS.

To further evaluate the noise-suppression capability of the STNN, we conduct a controlled noise-injection experiment on the 25-5-3-well dataset. Gaussian noise is added to the raw multi-view features at progressively increasing levels, and the full model is compared with Variant-III (w/o STNN). As shown in Figure 11, the performance of both methods decreases as the noise level increases; however, the full model consistently outperforms Variant-III across all six evaluation metrics and exhibits a substantially slower rate of degradation. These trends support the role of the STNN as a low-pass filter in the tensor spectral domain: it suppresses transient high-frequency disturbances while retaining low-frequency components associated with continuous macroscopic geological trends.

Table 6. Ablation results for the full model and four variants on five benchmark datasets. The best results are highlighted in **bold**.

Dataset	Model	ACC	NMI	Purity	F-score	Precision	ARI
Volcanic	Variant-I	72.64	65.87	81.89	71.48	76.83	62.99
	Variant-II	48.90	40.61	65.64	48.73	52.50	33.52
	Variant-III	37.26	16.44	47.52	31.73	33.09	10.61
	Variant-IV	74.85	71.52	82.60	72.89	77.80	64.77
	Ours	**88.35**	**81.13**	**90.50**	**85.54**	**89.82**	**81.11**
Facies	Variant-I	57.35	59.15	68.22	50.14	55.52	42.34
	Variant-II	79.12	77.42	81.41	75.89	71.10	71.31
	Variant-III	22.87	0.31	23.08	26.11	15.02	0.08
	Variant-IV	72.01	74.23	76.25	67.56	64.50	61.52
	Ours	**79.38**	**77.46**	**81.58**	**75.97**	**71.31**	**71.41**
35-6-2-S-well	Variant-I	58.91	62.38	73.70	62.76	66.91	53.02
	Variant-II	59.06	61.04	73.03	59.25	65.46	49.06
	Variant-III	54.22	53.09	73.85	50.43	61.98	39.59
	Variant-IV	72.51	72.03	86.03	69.43	78.78	62.05
	Ours	**75.79**	**72.06**	**86.11**	**72.88**	**82.27**	**66.29**
25-5-3-well	Variant-I	71.55	67.48	85.61	69.01	75.92	59.85
	Variant-II	75.51	77.07	89.00	75.28	82.38	67.94
	Variant-III	36.21	0.95	36.57	40.37	25.30	0.50
	Variant-IV	81.88	74.55	84.68	82.02	83.68	76.15
	Ours	**87.58**	**83.12**	**91.17**	**87.26**	**88.23**	**83.06**
cigFacies	Variant-I	85.24	75.31	85.24	77.49	75.90	71.61
	Variant-II	51.97	39.36	56.98	45.47	44.94	31.38
	Variant-III	37.59	16.44	42.94	33.96	31.17	15.20
	Variant-IV	25.01	0.05	25.05	33.75	20.30	0.00
	Ours	**86.32**	**76.51**	**86.33**	**78.43**	**76.73**	**72.26**

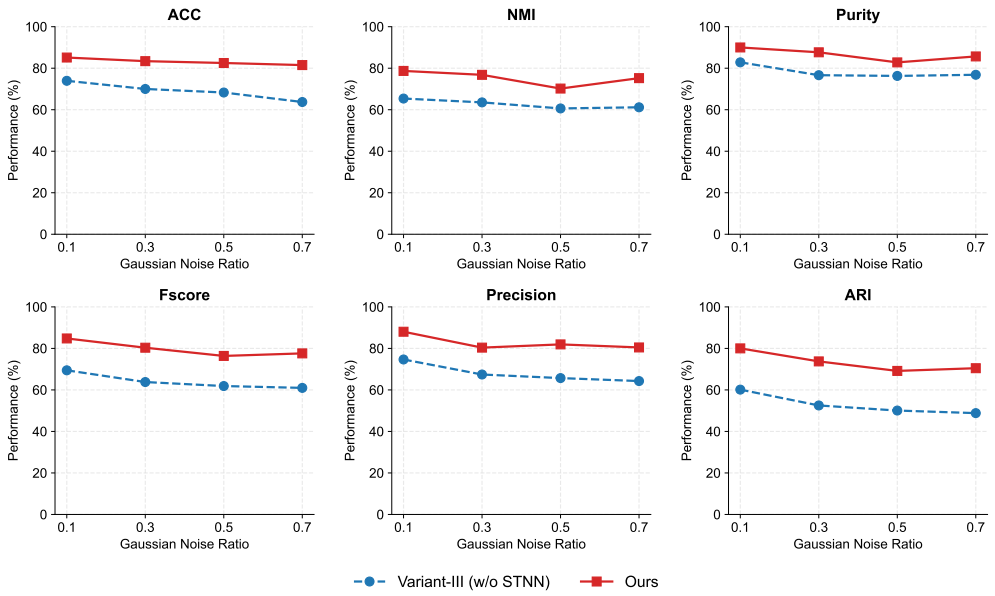


Figure 11. Robustness to different levels of Gaussian noise on the 25-5-3-well dataset: comparison of the full model and Variant-III (w/o STNN).

6. Conclusions

This paper presents Smooth Tensor Multi-View Clustering on Well Logs via Hypergraph Topology and Concurrent Group Sparsity (HTCGS) for heterogeneous well-log analysis. HTCGS uses a source-view hypergraph to propagate high-order semantic relationships and a cross-view concurrent joint-group-sparsity module to isolate synchronous downhole measurement errors. In addition, the Smooth Tensor Nuclear Norm (STNN) acts as a low-pass filter that suppresses high-frequency structural noise while preserving macroscopic geological trends. Experiments on five benchmark datasets show that HTCGS outperforms six recent representative baselines in terms of clustering accuracy and robustness. These findings provide geoscientists with a practical reference for integrating heterogeneous well-log measurements, identifying lithofacies, and obtaining reliable interpretations under complex downhole conditions. Future work focuses on extending HTCGS to incomplete multi-view settings involving missing or unpaired views across geological depth intervals and investigating adaptive view-weight learning so that each view can contribute to the final consensus according to its reliability and information content.

Author Contributions: Methodology, S.X., H.Z. and W.G.; Software, L.T. and Y.Z.; Validation, L.W., J.W. and L.T.; Formal analysis, S.X. and L.W.; Investigation, Y.Z. and J.W.; Data curation, L.W. and Y.Z.; Writing—original draft, S.X.; Writing—review and editing, H.Z., S.X. and W.G.; Visualization, J.W. and Y.Z.; Supervision, H.Z. and W.G.; Project administration, S.X.; Funding acquisition, S.X. All authors have read and agreed to the published version of the manuscript.

Funding: This research is supported by the Science and Technology Project of China National Petroleum Corporation (CNPC) (Grant Nos. 2023ZZ24 and 2023ZZ15), the Key Scientific and Technological Tackling Project of Xinjiang Oilfield, China National Petroleum Corporation (Grant No. 2024XJZD06), and the "Strategic Talents" Outstanding Engineer Program of the Xinjiang Uygur Autonomous Region (Grant No. XJRC-2025-GX-PY-GCS-013).

Data Availability Statement: The raw data supporting the conclusions of this article will be made available by the authors on request.

Conflicts of Interest: Shengjiang Xu, Liwei Wang, Long Tian, Yinming Zhong, and Junshan Wang are employed by the Oil Production Technology Research Institute, Xinjiang Oilfield Company. The authors declare that this study was conducted in the absence of any other commercial or financial relationships that could be construed as a potential conflict of interest.

References

1. Liang, J.; Dong, X.; Wang, P.; Xu, J.; Wu, D.; Nie, F. Multi-View Graph Clustering via Dual View-Cluster-Order Interactivity Mining. *IEEE Trans. Circuits Syst. Video Technol.* **2026**, *36*, 379–392. [CrossRef]
2. Qiang, Q.; Zhang, B.; Hua, Y.; Nie, F. Multi-View Clustering via Bilaterally Constrained Anchor Graph. *IEEE Trans. Pattern Anal. Mach. Intell.* **2026**, *48*, 9064–9077. [CrossRef] [PubMed]
3. Shi, S.; Zhang, X.; Zhang, C.; Nie, F. Comprehensive Multi-View Clustering via Low-Dimensional Subspace Representation. *IEEE Trans. Emerg. Top. Comput. Intell.* **2026**, 1–12. [CrossRef]
4. Li, Y.; Pan, B.; Guo, Y.; Zhang, L.; Guan, Y.; Wang, Q.; Wang, X.; Zhang, P. A multi-view learning approach for lithology identification with incomplete logging datasets. *J. Geophys. Eng.* **2026**, *23*, 444–455. [CrossRef]
5. Han, J.; Wang, S.; Cao, Z.; Li, J.; Liu, M. Multi-view and multi-scale super-resolution method of logging curves based on fractal theory. *Rev. Sci. Instrum.* **2022**, *93*, 124501. [CrossRef] [PubMed]
6. Tan, H.; Wan, Y.; Luo, G.; Sun, Z. Hierarchical Multi-View Representation Learning via Generalized Deep Non-Negative Matrix Factorization. *Mathematics* **2026**, *14*, 1442. [CrossRef]
7. Phoka, T.; Poonprapan, P.; Boriwan, P. A Heuristic Approach to Competitive Facility Location via Multi-View K-Means Clustering with Co-Regularization and Customer Behavior. *Mathematics* **2025**, *13*, 2481. [CrossRef]
8. Zhang, Y.; Wu, J.; Zhou, C.; Cai, Z.; Yang, J.; Yu, P.S. Multi-View Fusion with Extreme Learning Machine for Clustering. *ACM Trans. Intell. Syst. Technol.* **2019**, *10*, 1–23. [CrossRef]

9. Wang, X.; Zhang, Y.; Zhou, Y. Bidirectional Probabilistic Multi-Graph Learning and Decomposition for Multi-View Clustering. *IEEE Trans. Image Process.* **2025**, *34*, 3609–3621. [CrossRef] [PubMed]
10. Yuan, Z.; Yang, Z.; Cai, Y.; Wu, K.; Liu, M.; Zhang, D.; Jiang, H.; Li, Z.; Wang, Z. SED-MVS: Segmentation-Driven and Edge-Aligned Deformation Multi-View Stereo With Depth Restoration and Occlusion Constraint. *IEEE Trans. Circuits Syst. Video Technol.* **2025**, *35*, 11244–11257. [CrossRef]
11. Shen, H.; Zhuang, P.; Kou, J.; Zeng, Y.; Xu, H.; Li, J. MGD-SAM2: Multi-View Guided Detail-Enhanced Segment Anything Model 2 for High-Resolution Class-Agnostic Segmentation. *IEEE Trans. Circuits Syst. Video Technol.* **2026**, *36*, 11503–11516. [CrossRef]
12. Wang, E.; Chen, S.; Zhang, X.; Zhou, Y.; Ren, Z. Consistency alignment via reliability-aware multi-view subspace clustering. *Inf. Sci.* **2026**, 123833. [CrossRef]
13. Shi, L.; Ye, Y.; Cao, L.; Zhao, Y.; Chen, B. Tensor-Based Graph Learning With Consistency and Specificity for Multi-View Clustering. *IEEE Trans. Multimed.* **2026**, *28*, 1562–1575. [CrossRef]
14. Kong, Z.; Chang, D.; Wang, Y.; Li, P.; Zhao, Y. Tensorial Multi-View Clustering via Alternative Rank Minimization and Inter-View Alignment. *IEEE Trans. Knowl. Data Eng.* **2026**, *38*, 3196–3209. [CrossRef]
15. Wu, H.; Dai, Y.J.; Liu, X.Y. Efficient Sedimentary Facies Recognition Using Vision Transformer and Weakly Supervised Deep Multi-View Clustering. *IEEE Access* **2025**, *13*, 77522–77538. [CrossRef]
16. Ali, M.; Zhu, P.; Jiang, R.; Huolin, M.; Ashraf, U.; Zhang, H.; Hussain, W. Data-driven lithofacies prediction in complex tight sandstone reservoirs: A supervised workflow integrating clustering and classification models. *Geomech. Geophys. Geo-Energy Geo-Resour.* **2024**, *10*, 70. [CrossRef]
17. Hasan, M.M.U.; Hasan, T.; Shahidi, R.; James, L.; Peters, D.; Gosine, R. Lithofacies identification from wire-line logs using an unsupervised data clustering algorithm. *Energies* **2023**, *16*, 8116. [CrossRef]
18. Tian, L.; Zhu, Z.; Wang, L.; Yu, J.; Wang, Y. A Rock Drillability Characterization Method Based on Big Data and Unsupervised Clustering Algorithm. *Xinjiang Oil Gas* **2024**, *20*, 29–36.
19. Yang, Z.; Teng, J.; Wang, X.; Xu, M.; Li, J.; Guo, J.; Liu, Y. Research Progress and Prospect of Sweet Spot Prediction and Evaluation Methods for Shale Reservoirs. *Xinjiang Oil Gas* **2026**, *22*, 57–65.
20. Song, X.; Wang, Y.; Yang, Y.; Liu, M.; Zhu, Z. Intelligent Diagnosis and Analysis of Stuck Pipe Based on Supervised and Unsupervised Algorithms. *Xinjiang Oil Gas* **2025**, *21*, 24–34.
21. Zhang, Y.; Yang, Y.; Zhang, W.; Liu, M.; Zhu, Z.; Wang, Y. An Intelligent Prediction Method for Drilling Stuck Risk Based on Mechanism Data Fusion. *Xinjiang Oil Gas* **2025**, *21*, 35–44.
22. Meng, K.; He, S.; Bao, H.; Meng, X.; Zhao, T.; Cao, B.; Luo, X.; Johnson, L.; Yu, H. Identification of shale lithofacies by well logs based on clustering algorithms. *Acta Geophys.* **2025**, *73*, 3257–3269. [CrossRef]
23. Zhang, L.; He, J.; Chen, L.; Mao, Z.; Shi, B. Multidimensional adaptive deep clustering for intelligent diagenetic facies logging recognition. *SPE J.* **2025**, *30*, 1614–1628. [CrossRef]
24. Yang, X.; Dong, S.; Quan, J.; Xu, T.; Kong, H.; Zeng, L.; Xiong, G.; Bi, R. Lithology identification using stratigraphic continuity and petrophysical features of well logs. *Results Eng.* **2026**, *29*, 109913. [CrossRef]
25. Xu, Z.; Liu, H.; Lang, C.; Wang, T.; Li, Y.; Kampffmeyer, M.C. A hubness perspective on representation learning for graph-based multi-view clustering. In *Proceedings of the 2025 IEEE/CVF Conference on Computer Vision and Pattern Recognition (CVPR)*; IEEE: Piscataway, NJ, USA, 2025; pp. 15528–15537.
26. Dong, W.; Wu, X.J.; Fan, B. Anchor point segmentation based multi-view clustering. *Neural Netw.* **2025**, *194*, 108175. [CrossRef] [PubMed]
27. Liu, X.; Wang, Q.W.; Chen, J.F. Multi-View Clustering via Projection-Enhanced Bipartite Graph Learning and Consensus Fusion. *Mathematics* **2026**, *14*, 1767. [CrossRef]
28. Zhao, W.; Li, G.; Yang, H.; Gao, Q.; Wang, Q. Embedded feature selection on graph-based multi-view clustering. *Proc. Proc. AAAI Conf. Artif. Intell.* **2024**, *38*, 17016–17023. [CrossRef]
29. Wang, B.; Wang, J.; Zeng, C.; Chen, M. Locality-driven flexible consensus graph learning for multi-view clustering. *Pattern Recognit.* **2026**, *169*, 111853. [CrossRef]
30. Wang, J.; Deng, T.; Ran, Y.; Yang, M.; Liu, X. Embedded Multi-View Clustering via Fusing Tensor Subspace Representation and Adaptive Graph Learning. *IEEE Trans. Circuits Syst. Video Technol.* **2026**, *36*, 8631–8645. [CrossRef]
31. Cai, B.; Dai, P.; Wang, S.; Lu, G.F. Robust contrastive multi-view subspace clustering. *Pattern Recognit.* **2026**, *179*, 113696. [CrossRef]
32. Li, J.; Zhang, X.; Wang, J.; Sun, H. Simultaneously learning representation tensor and orthogonal projection for multi-view subspace clustering. *Neurocomputing* **2026**, *698*, 134255. [CrossRef]
33. Ding, M.; Yang, J.H.; Zhao, X.L.; Zhang, J.; Ng, M.K. Nonconvex Low-Rank Tensor Representation for Multi-View Subspace Clustering With Insufficient Observed Samples. *IEEE Trans. Knowl. Data Eng.* **2025**, *37*, 3583–3597. [CrossRef]
34. Xu, K.; Chen, L.; Wang, S. Toward Robust Nonlinear Subspace Clustering: A Kernel Learning Approach. *IEEE Trans. Artif. Intell.* **2026**, *7*, 726–739. [CrossRef]

35. Chen, Z.; Wu, X.J.; Xu, T.; Li, H.; Kittler, J. Multi-layer multi-level comprehensive learning for deep multi-view clustering. *Inf. Fusion* **2025**, *116*, 102785. [CrossRef]
36. Yan, W.; Yang, T.; Tang, C. Self-Supervised Semantic Soft Label Learning Network for Deep Multi-View Clustering. *IEEE Trans. Multimed.* **2025**, *27*, 4971–4983. [CrossRef]
37. Zhang, Y.; Cai, J.; Wu, Z.; Wang, P.; Ng, S.K. Mixture of experts as representation learner for deep multi-view clustering. *Proc. Proc. AAAI Conf. Artif. Intell.* **2025**, *39*, 22704–22713. [CrossRef]
38. Xiao, B.; Dong, Z.; Liang, K.; Liu, S.; Wang, S.; Liu, T.; Hu, X.; Zhu, E.; Liu, X. EASEMVC: Efficient Dual Selection Mechanism for Deep Multi-View Clustering. In *Proceedings of the Computer Vision and Pattern Recognition Conference*; IEEE: Piscataway, NJ, USA, 2025; pp. 20716–20726.
39. Cui, J.; Wu, X.; Zhang, H.; Dong, C.; Wen, J. Structure-guided deep multi-view clustering. *Inf. Fusion* **2026**, *125*, 103461. [CrossRef]
40. Long, Z.; Liu, Y.; Ren, Y.; Zhu, C. SLR-MVTC: Smooth Low-Rank Multi-View Tensor Clustering. *Proc. Proc. AAAI Conf. Artif. Intell.* **2025**, *39*, 19095–19103. [CrossRef]
41. Boyd, S.; Parikh, N.; Chu, E.; Peleato, B.; Eckstein, J. Distributed optimization and statistical learning via the alternating direction method of multipliers. *Found. Trends Mach. Learn.* **2011**, *3*, 1–122. [CrossRef]
42. Liu, G.; Lin, Z.; Yan, S.; Sun, J.; Yu, Y.; Ma, Y. Robust Recovery of Subspace Structures by Low-Rank Representation. *IEEE Trans. Pattern Anal. Mach. Intell.* **2013**, *35*, 171–184. [CrossRef] [PubMed]
43. Gao, H.; Wu, X.; Sun, X.; Hou, M.; Gao, H.; Wang, G.; Sheng, H. CigFacies: A massive-scale benchmark dataset of seismic facies and its application. *Earth Syst. Sci. Data* **2025**, *17*, 595–609. [CrossRef]
44. Zhang, J.; Yu, S.; Liu, S.; Wang, S.; Li, M.; Liu, X.; Zhu, E.; He, K. Learning the Anchors with Similar Distributions to Original Data for Multi-view Clustering. In *Proceedings of the 33rd ACM International Conference on Multimedia*; Association for Computing Machinery: New York, NY, USA, 2025; pp. 857–866.
45. Wang, J.; Li, M.; Li, Z.; Yu, H.; Liu, S.; Hu, D.; Tang, C.; Liu, X. Tensor Multi-Rank Constraint Guided Anchor-Wise Adaptive Alignment for Multi-View Clustering. *IEEE Trans. Knowl. Data Eng.* **2026**, *38*, 2015–2027. [CrossRef]
46. Wang, Z.; Liu, Z.; Hu, D.; Jia, T. Nonconvex Multiview Subspace Clustering Framework with Efficient Method Designs and Theoretical Analysis. In Proceedings of the Thirty-Third International Joint Conference on Artificial Intelligence Main Track, Jeju, Korea, 3–9 August 2024; pp. 5162–5170.
47. Wan, X.; Liu, J.; Gan, X.; Liu, X.; Wang, S.; Wen, Y.; Wan, T.; Zhu, E. One-Step Multi-View Clustering With Diverse Representation. *IEEE Trans. Neural Netw. Learn. Syst.* **2025**, *36*, 5774–5786. [CrossRef] [PubMed]
48. Liu, S.; Liao, Q.; Wang, S.; Liu, X.; Zhu, E. Robust and Consistent Anchor Graph Learning for Multi-View Clustering. *IEEE Trans. Knowl. Data Eng.* **2024**, *36*, 4207–4219. [CrossRef]
49. Zhao, M.; Nie, F.; Wang, C.; Li, X.; Tan, Z.; Hu, H. Nonnegative Spectral Embedding Learning with Adaptive Neighbors for Multi-view Clustering. *Neural Netw.* **2026**, *197*, 108537. [CrossRef] [PubMed]

Disclaimer/Publisher's Note: The statements, opinions and data contained in all publications are solely those of the individual author(s) and contributor(s) and not of MDPI and/or the editor(s). MDPI and/or the editor(s) disclaim responsibility for any injury to people or property resulting from any ideas, methods, instructions or products referred to in the content.